Journal of Southeast University (English Edition) Vol. 40, No. 4, pp. 372 – 385 Dec. 2024 ISSN 1003—7985

Optimizing data for electrical resistivity tomography in hardened sites through the ratio method

Jiang Fuyu[1] Gao Likun[2] Chen Haijun[3] Ni Jiong[1] Li Fuqiang[4]

([1] School of Earth Sciences and Engineering, Hohai University, Nanjing 211100, China)
([2] The First Geological Brigade of Jiangsu Geology and Mineral Resources Bureau, Nanjing 210041, China)
([3] Nanjing Hydraulic Research Institute, Nanjing 210029, China)
([4] China Energy Engineering Group Hunan Electric Power Design Institute Co., Ltd., Changsha 410007, China)

Abstract: To reduce the shielding effect of hardened layers on electrical resistivity tomography, a ratio method based on the distortion correction principle and the isolation coefficient is proposed. The effects of the resistivity and thickness of hardened concrete layers on the detection of target objects are explored. Both numerical simulations and indoor tank tests indicate that when the ratio method is employed to correct the original collected data, the maximum allowable error for the isolation coefficient should not exceed 1%. Notably, when the ratio of hardened layer thickness to electrode spacing does not exceed 1, correction through this method significantly enhances the recognition capability of target objects. However, when the hardened layer thickness is greater than the electrode spacing by a factor of 2 or more, the ratio method cannot achieve satisfactory results. The case study of flood control engineering detection in the Zhangxi section of the Huangpen River in Dongzhi County demonstrates that the detection effect after correction by the ratio method is comparable to that for the adjacent unhardened pavement, and the influence of the hardened layer is obviously weakened, resulting in more reliable results.

Key words: ratio method; resistivity tomography; hardened site; distortion principle; data optimization

DOI: 10.3969/j.issn.1003 – 7985.2024.04.006

The resistivity parameters of underground rock and soil play a vital role in assessing the quality of geological formations and in mineral resource exploration. Geologists and geophysicists have consistently focused on these parameters owing to their significance in understanding subsurface structure and composition.

Between 1920 and the mid-1980s, the resistivity method primarily functioned as a one-dimensional mapping technique pioneered by Schlumberger[1]. However, in 1987, Shima and Sakayama[2] introduced electrical resistivity tomography (ERT), revolutionizing the detection of geoelectric structures by enabling multi-directional and short-distance measurements. Over the past 30 years, the ERT method has undergone significant development. Data acquisition instruments have transitioned from centralized to distributed systems and from single-channel to multi-channel configurations[3-7]. Similarly, data collection techniques have advanced significantly, shifting from one-dimensional to four-dimensional measurements and expanding from surface observations to cross-well and surface-well observations[8-12].

The ERT method has been widely employed in engineering and environmental surveys, hydrogeological research, mineral resource exploration, agricultural and soil science, archaeology and cultural heritage, seawater intrusion, and various other fields[13-23]. The method plays an indispensable role in detecting adverse geological features during the early stages of engineering construction, conducting quality inspections throughout the construction process, and providing precise detection during operation periods, thereby ensuring the construction and safe operation of major national projects.

With the advancement of the economy and society, the ERT method has found increasing practical application across various sectors, including water conservancy and hydropower engineering, environmental engineering, and municipal engineering. In most of the application sites, the ground has undergone concrete hardening. To establish coupling between the power supply (or measuring) electrodes and the pavement, methods such as the use of soil bags and grounding cans are commonly employed[24-26]. Unfortunately, while this approach resolves the issue of data acquisition, it cannot effectively identify targets located beneath the hardened layer owing to the shielding effect of the high-resistivity surface layer and the rapid attenuation of electrical signals as they penetrate deeper.

To mitigate the impact of concrete-hardened road surfaces on the detection effectiveness of the ERT method, this study investigates the influence of the resistivity and thicknesses of concrete layers on the detection of target bodies according to distortion correction principles[27-29]. A ratio method, which incorporates an isolation coeffi-

Received 2024-01-04, **Revised** 2024-04-01.

Biography: Jiang Fuyu (1981—), male, doctor, associate professor, jiangfy@hhu.edu.cn.

Foundation item: National Key Research and Development Program of China (No. 2021YFC3000103).

Citation: Jiang Fuyu, Gao Likun, Chen Haijun, et al. Optimizing data for electrical resistivity tomography in hardened sites through the ratio method[J]. Journal of Southeast University (English Edition), 2024, 40(4): 372 – 385. DOI: 10.3969/j.issn.1003 – 7985.2024.04.006.

cient to mitigate the shielding effect of the hardened layer, is proposed. This research offers a clear direction for the application and data processing of the ERT method in concrete-hardened sites.

1 Ratio Correction and Inversion Method

1.1 Ratio correction principle

When power is supplied at points A and B, the current density j_{MN} between the measuring electrodes M and N is expressed as follows:

$$j_{MN} = j_0 + \Delta j_{\text{dis}} + \Delta j_{\text{obj}} \tag{1}$$

where j_0 represents the current density when the surface is horizontal, and the underground medium is uniform and isotropic; Δj_{obj} represents the change in current density caused by the target body; and Δj_{dis} represents the distortion in current density at M and N due to the interference (hardened concrete layer). From Eq. (1), the following equation can be derived:

$$\frac{j_{MN}}{j_0} = \frac{j_0 + \Delta j_{\text{dis}}}{j_0} \frac{j_0 + \Delta j_{\text{dis}} + \Delta j_{\text{obj}}}{j_0 + \Delta j_{\text{dis}}} \tag{2}$$

According to the relation between the apparent resistivity ρ_{a}, resistivity of measuring electrodes ρ_{MN}, and current density:

$$\rho_{\text{a}} = \frac{j_{MN}}{j_0} \rho_{MN} \tag{3}$$

By substituting Eq. (3) into Eq. (2) and setting $\rho_{MN} = \rho_0$, we obtain

$$\frac{\rho_{\text{a}}^{\text{mix}}}{\rho_0} = \frac{\rho_{\text{a}}^{\text{dis}}}{\rho_0} \frac{j_0 + \Delta j_{\text{dis}} + \Delta j_{\text{obj}}}{j_0 + \Delta j_{\text{dis}}} \tag{4}$$

where $\rho_{\text{a}}^{\text{mix}}$ represents the measured apparent resistivity; $\rho_{\text{a}}^{\text{dis}}$ represents the apparent resistivity induced by the interference; and ρ_0 represents the surrounding rock resistivity.

Generally, the current density Δj_{obj} induced by the target body is directly proportional to the current density j_0 induced by the surrounding rock. Then,

$$\Delta j_{\text{obj}} = k j_0 \tag{5}$$

where k represents the anomaly coefficient, which is related to the size, shape, and resistivity of the target body. When there is only a target body underground,

$$\frac{\rho_{\text{a}}^{\text{obj}}}{\rho_0} = \frac{j_0 + \Delta j_{\text{obj}}}{j_0} = \frac{j_0 + k j_0}{j_0} = 1 + k \tag{6}$$

where $\rho_{\text{a}}^{\text{obj}}$ denotes the apparent resistivity attributed to the target body. Under the assumption that the current density induced by the interference and surrounding rock at M and N is designated as j_0', equivalent to $j_0 + \Delta j_{\text{dis}}$, the current density induced by the target against the backdrop of the interference and the surrounding rock is denoted as kj_0'. Consequently, the second term of Eq. (4) can be expressed as follows:

$$\frac{j_0 + \Delta j_{\text{dis}} + \Delta j_{\text{obj}}}{j_0 + \Delta j_{\text{dis}}} = \frac{j_0 + \Delta j_{\text{dis}} + k(j_0 + \Delta j_{\text{dis}})}{j_0 + \Delta j_{\text{dis}}} = 1 + k \tag{7}$$

By substituting Eqs. (6) and (7) into Eq. (4),

$$\frac{\rho_{\text{a}}^{\text{mix}}}{\rho_0} = \frac{\rho_{\text{a}}^{\text{dis}}}{\rho_0} \frac{\rho_{\text{a}}^{\text{obj}}}{\rho_0} \tag{8}$$

Therefore, we obtain the revised formula for apparent resistivity,

$$\rho_{\text{a}}^{\text{obj}} = \frac{\rho_0 \rho_{\text{a}}^{\text{mix}}}{\rho_{\text{a}}^{\text{dis}}} \tag{9}$$

In practical application, $\rho_{\text{a}}^{\text{dis}}$ denotes the computed forward value of interference, and it can be obtained through methods such as the finite element or finite difference techniques.

1.2 Least-squares inversion method

The aim of the optimization inversion method is to minimize the disparity between the calculated and measured apparent resistivity values through adjustments to the resistivity of model blocks, subject to the smoothness constraints applied. This disparity is quantified in terms of the root-mean-square error. The inversion routine employed by the software Res2dinv is based on the smoothness-constrained least-squares method[30], which is defined by the following equation:

$$(\boldsymbol{J}^{\text{T}}\boldsymbol{J} + \lambda \boldsymbol{F})\,\Delta \boldsymbol{q}_k = \boldsymbol{J}^{\text{T}}\boldsymbol{g} - \lambda \boldsymbol{F}\boldsymbol{q}_k \tag{10}$$

where $\boldsymbol{F} = \alpha_x \boldsymbol{C}_x^{\text{T}}\boldsymbol{C}_x + \alpha_z \boldsymbol{C}_z^{\text{T}}\boldsymbol{C}_z$, $\boldsymbol{C}_x$ represents horizontal roughness filters; $\boldsymbol{C}_z$ represents vertical roughness filter; $\boldsymbol{J}$ is the Jacobian matrix of partial derivatives; λ is the damping factor; $\boldsymbol{q}_k$ is the model change vector; and $\boldsymbol{g}$ represents the data misfit vector.

One advantage of this method is that the damping factor and roughness filters can be adjusted to suit different data types.

2 Impact of Hardened Sites on Detection Results

A two-dimensional geoelectric model for the ERT method under hardened site conditions was established using the COMSOL Multiphysics coupled finite element software and the stable point current source electric field as the starting point. The target anomaly was depicted as a circular body with low resistivity (or high resistivity) and a diameter of 2 m, and potential near-circular leakage channels (or cavities) were simulated. Both the power supply electrodes and measuring electrodes were positioned on the surface of the hardened concrete layer.

During the numerical simulation, a total of 60 electrodes were employed for the ERT method, with an electrode spacing of 1 m. The burial depth of the top of the anomaly, h_{top}, was varied as 1.0, 4.0, and 7.0 m, while the thickness of the hardened layer, h_c, was set to 0.1, 0.3, 0.5, 0.8, and 1.0 m. The resistivity values for the low-resistivity, high-resistivity, and surrounding rocks were set to 10, 1 000, and 200 Ω · m, respectively.

Concrete typically utilized in hardened concrete sites falls within the strength range of C20 to C30, and the resistivity value of the concrete is closely related to the surrounding environment. In this numerical simulation, the resistivity of the hardened concrete layer was established at 500 Ω · m, based on research findings cited in Refs. [31 − 32].

2.1 Different arrays

To explore the influence of hardened concrete layers on the detection capabilities of various array types, numerical simulations were conducted using Wenner, dipole, and differential arrays for different types of target bodies. Fig. 1 illustrates the inversion results of the ERT method for circular low-resistivity and high-resistivity models with a radius of 1 m, h_c of 0.3 m, and h_{top} of 4.0 m, processed using the Res2dinv software (all subsequent inversion images in this study were processed using this software). In Fig. 1, the black circles denote the actual locations of the anomalies. As depicted in Fig. 1, owing to the influence of the high-resistivity hardened layer, both the low-resistivity and high-resistivity models exhibit a two-layer structure in the resistivity inversion results of the three devices, with higher resistivity values in the upper layer and lower resistivity values in the lower layer. The surface resistivity reflects a relatively high-resistivity zone, and the horizontal location of the target anomaly ranges from 26 to 34 m.

Regarding the low-resistivity model, the Wenner array inversion results reveal an anomaly depth ranging from approximately 2 to 9 m, displaying a shape resembling an hourglass. The resistivity values fall within the range of 132 to 144 Ω · m. Although the hourglass's neck roughly aligns with the actual location of the low-resistivity body, its size and shape notably deviate from the real conditions (see Fig. 1(a)). This disparity is attributable to the combined influence of shielding and volume effects within the hardened layer.

For the differential array, the inverted anomaly depth ranges from approximately 1.5 to 5.0 m, and the inverted anomaly exhibits a nearly elliptical shape. The resistivity values range between 170 and 185 Ω · m. Notably, the center of the relatively low-resistivity anomaly is notably higher than the actual position of the low-resistivity body (see Fig. 1(c)).

In the case of the dipole array, the inversion depth ranges from approximately 2 to 7 m, presenting a nearly circular shape. The resistivity values fall within the range of 160 to 180 Ω · m. The center of the low-resistivity anomaly closely matches the actual position of the low-resistivity body (see Fig. 1(e)).

In comparison, the high-resistivity anomaly model is accurately represented in all three arrays, attributed to the low-resistivity characteristics of the surrounding rock. However, in terms of resolution, the dipole array demonstrates the most effective performance (see Figs. 1(e), (f)). Consequently, the dipole array is used as the primary example for discussion in subsequent sections.

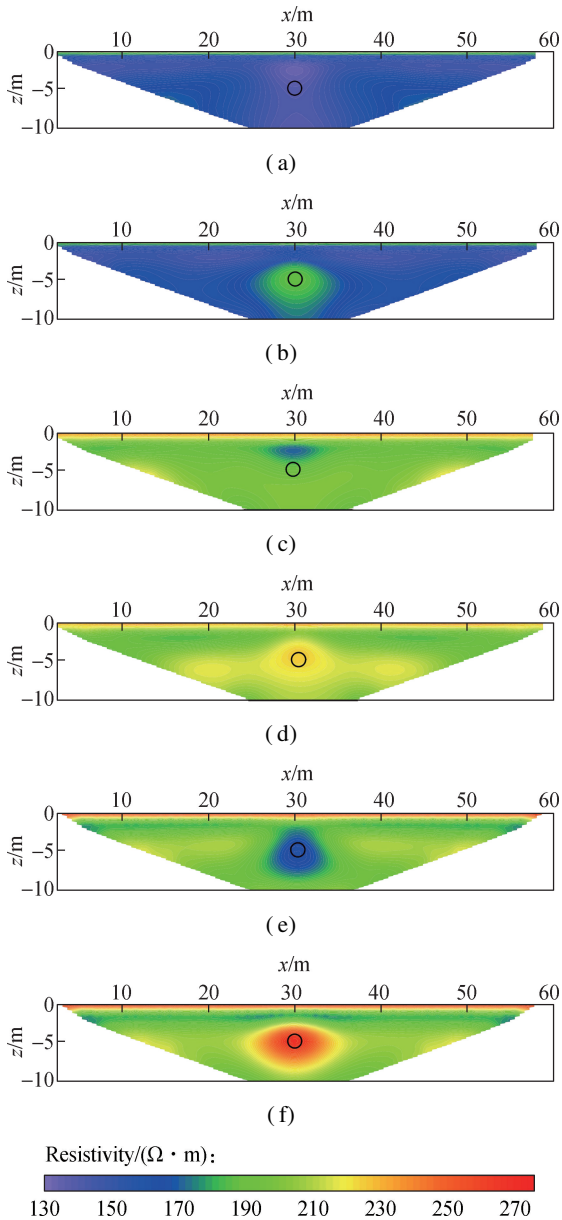

Fig. 1 Inversion results of low-resistivity and high-resistivity anomaly models based on different array types with hardened layers. (a) Low-resistivity model based on the Wenner array; (b) High-resistivity model based on the Wenner array; (c) Low-resistivity model based on the differential array; (d) High-resistivity model based on the differential array; (e) Low-resistivity model based on the dipole array; (f) High-resistivity model based on the dipole array

2.2 Difference in hardened layer thickness and abnormal body buried depth

Figs. 2 and 3 illustrate the inversion results for both low- and high-resistivity models, considering various h_c values (0, 0.3, 0.5, and 1.0 m) and h_{top} values (1.0, 4.0, and 7.0 m). As the thickness of the hardened layer increases, the resistivity obtained from the inversion demonstrates a consistent upward trend.

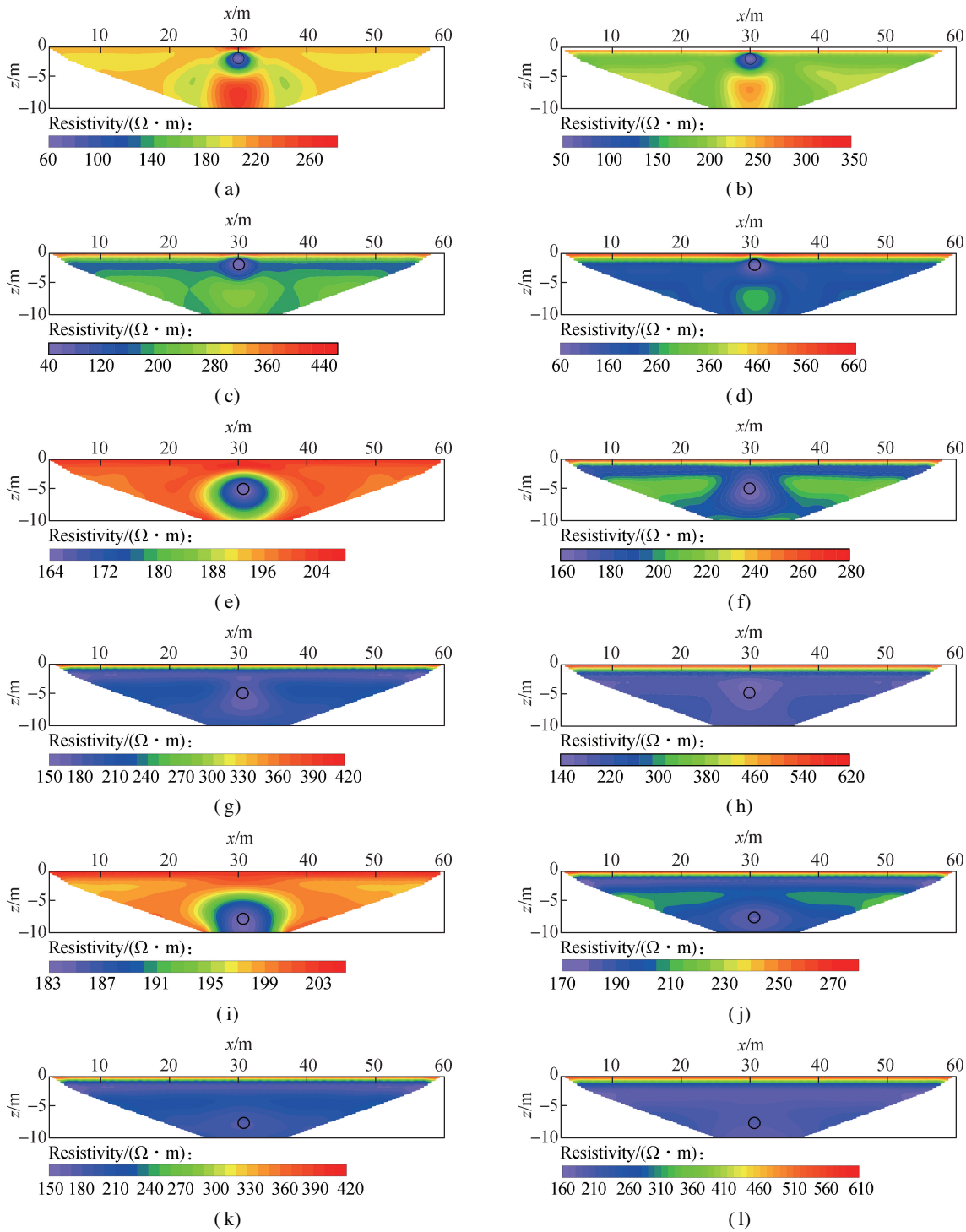

Fig. 2 Inversion results of low-resistivity anomaly model with different thicknesses of the hardened layer and varying buried depths of the anomaly body. (a) h_{top} = 1.0 m, h_c = 0 m; (b) h_{top} = 1.0 m, h_c = 0.3 m; (c) h_{top} = 1.0 m, h_c = 0.5 m; (d) h_{top} = 1.0 m, h_c = 1.0 m; (e) h_{top} = 4.0 m, h_c = 0 m; (f) h_{top} = 4.0 m, h_c = 0.3 m; (g) h_{top} = 4.0 m, h_c = 0.5 m; (h) h_{top} = 4.0 m, h_c = 1.0 m; (i) h_{top} = 7.0 m, h_c = 0 m; (j) h_{top} = 7.0 m, h_c = 0.3 m; (k) h_{top} = 7.0 m, h_c = 0.5 m; (l) h_{top} = 7.0 m, h_c = 1.0 m

At h_{top} = 1.0 m, the inverted low-resistivity anomalies closely match the actual buried depth and location (see Figs. 2(a)-(d)). However, with an increase in h_{top} to 4.0 m, the resolution of the ERT method deteriorates rapidly

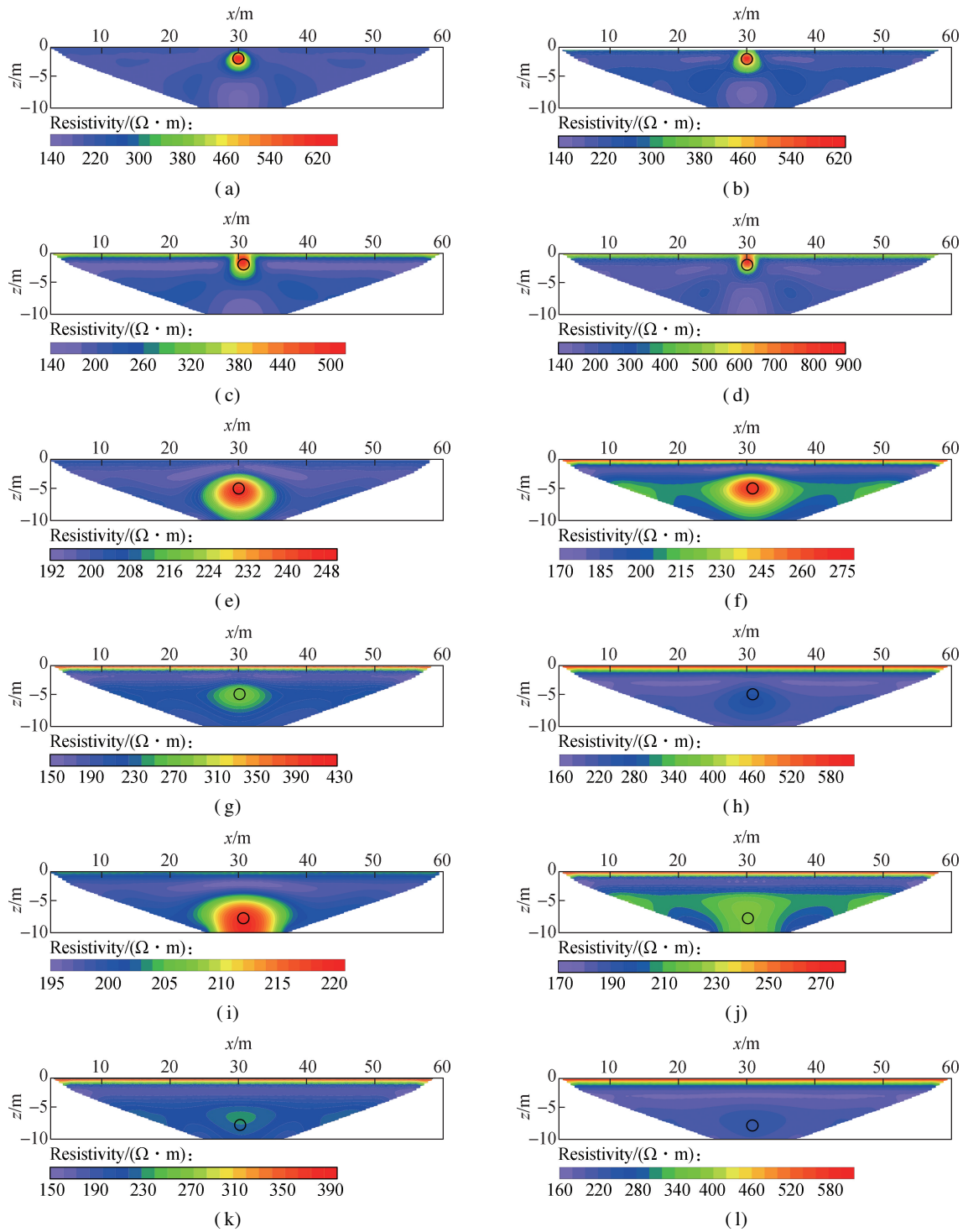

Fig. 3 Inversion results of high-resistivity anomaly model with different thicknesses of the hardened layer and varying buried depths of the anomaly body. (a) h_{top} = 1.0 m, h_c = 0 m; (b) h_{top} = 1.0 m, h_c = 0.3 m; (c) h_{top} = 1.0 m, h_c = 0.5 m; (d) h_{top} = 1.0 m, h_c = 1.0 m; (e) h_{top} = 4.0 m, h_c = 0 m; (f) h_{top} = 4.0 m, h_c = 0.3 m; (g) h_{top} = 4.0 m, h_c = 0.5 m; (h) h_{top} = 4.0 m, h_c = 1.0 m; (i) h_{top} = 7.0 m, h_c = 0 m; (j) h_{top} = 7.0 m, h_c = 0.3 m; (k) h_{top} = 7.0 m, h_c = 0.5 m; (l) h_{top} = 7.0 m, h_c = 1.0 m

with depth. As the thickness of the concrete increases, the region reflecting the presence of abnormal bodies through relatively low-resistivity traps expands. Notably, when h_c reaches 0.5 m, a significant discrepancy exists between the center of the low-resistivity anomaly and the actual anomaly center, making it challenging to identify the relative minimum value (see Figs. 2 (e)-(h)).

At h_{top} = 7.0 m and h_c = 0.3 m, pinpointing the location of the low-resistivity body becomes challenging. Furthermore, at h_c = 1.0 m, it becomes impossible to discern the presence of a low-resistivity body (see Figs. 2 (i)-(l)).

Regarding the high-resistivity model, its detection effectiveness generally exceeds that of the low-resistivity

model, as evident in Fig. 3. This is primarily due to the relatively lower resistivity of the surrounding rock, which aids in current propagation. Consequently, the current density in the lower portion is higher than that of the low-resistivity model. Nevertheless, as the buried depth of the exploration target and the thickness of the hardened layer increase, identifying high-resistivity closed circles becomes increasingly challenging, and their positional deviations increase (see Figs. 3 (a)-(l)).

Numerical simulations conducted for both low- and high-resistivity models reveal that the shielding effect on detecting underground anomaly intensifies as the thickness of the hardened layer increases. Remarkably, when h_c reaches 1.0 m, considerable interference exists in the detection of smaller anomalous bodies. Conversely, the hardened layer exhibits minimal impact on the identification of shallow anomalies. However, as buried depth increases, the shielding effect of the hardened layer enhances the volume effect of ERT, leading to a rapid decline in the ability to recognize anomalous bodies. Consequently, achieving significant improvement in the detection accuracy of resistivity values obscured by high-resistivity shielding holds practical importance.

3 Discussion and Analysis of Correction Effect

3.1 Determination of correction layer

During the analysis of actual data, recognizing the significant decrease in current density with depth is crucial. Therefore, when evaluating the appropriate isolation coefficient and its effects, we utilize the apparent resistivity obtained from numerical simulations of various abnormal bodies without a hardening layer as our reference point. Subsequently, we conduct a statistical analysis on the rate of change of the apparent resistivity relative to this baseline, considering different resistivity levels and thicknesses of the hardening layer. This analysis enables us to quantitatively evaluate the consistency of these variations.

Table 1 presents a comprehensive overview of the rate of change in apparent resistivity compared with scenarios without a hardening layer. The table encompasses the impacts of different isolation coefficients, the resistivity of the hardening layer, and the ratio of hardening layer thickness to electrode distance. This comprehensive approach ensures a nuanced understanding of the correction effect and enables accurate determination of the correction layer.

Table 1 illustrates that the data change rate of the first layer beneath the hardened layer shows notable variations with the change in resistivity. Particularly, as the resistivity ranges from 500 to 1 600 Ω · m, the change rate varies approximately from 23.18% to 52.14%. In contrast, the disparities in change rates between the second and eighth layers gradually decrease, narrowing from 5.9% to 0.16%. Notably, no discernible difference in apparent resistivity of the ninth layer exists when resistivity of hardened layer changed from 500 to 1 600 Ω · m.

Table 1 Change in apparent resistivity rate with isolation coefficient, resistivity of hardened layer, and the ratio of the hardened layer thickness to the electrode distance %

Isolation coefficient	Resistivity of hardened layer /(Ω · m)					Ratio of hardened layer thickness to electrode distance				
	500	800	1 000	1 250	1 600	0.1	0.3	0.5	0.8	1.0
1	23.18	33.47	38.73	44.60	52.14	1.87	23.18	67.78	126.57	149.10
2	4.63	5.39	5.60	5.76	5.90	0.50	4.63	15.14	44.31	67.85
3	2.33	2.71	2.82	2.90	2.96	0.37	2.33	6.37	18.20	30.20
4	1.64	1.95	2.04	2.11	2.17	0.33	1.64	3.94	9.96	16.19
5	1.20	1.43	1.50	1.56	1.60	0.27	1.20	2.73	6.40	10.07
6	0.84	0.99	1.04	1.08	1.11	0.19	0.84	1.89	4.36	6.74
7	0.55	0.64	0.67	0.69	0.70	0.11	0.55	1.28	3.01	4.65
8	0.32	0.36	0.37	0.38	0.38	0.05	0.32	0.82	2.04	3.22
9	0.16	0.17	0.17	0.17	0.16	0.01	0.16	0.50	1.38	2.24
10	0.05	0.03	0.02	0.01	0.01	0.02	0.05	0.27	0.90	1.54
11	0.02	0.05	0.06	0.07	0.08	0.04	0.02	0.12	0.58	1.07
12	0.06	0.10	0.12	0.13	0.14	0.05	0.06	0.02	0.36	0.74
13	0.09	0.12	0.14	0.15	0.16	0.05	0.09	0.03	0.23	0.52
14	0.10	0.13	0.15	0.16	0.17	0.05	0.10	0.06	0.13	0.37
15	0.10	0.13	0.15	0.16	0.17	0.05	0.10	0.08	0.08	0.27
16	0.08	0.10	0.11	0.12	0.13	0.04	0.08	0.07	0.02	0.15

Moreover, when the isolation coefficient exceeds 9, the apparent resistivity change rate becomes negligible, indicating a stabilizing trend with a change rate below 0.20%. Additionally, under a constant electrode distance, the resistivity change rate varies notably with the thickness of the hardened layer. As the ratio of hardened layer thickness to electrode distance increases from 0.1 to 1.0, the rate of change in resistivity compared to the condition without a hardened layer rises from 1.87% to 149.10%.

In general, with two maximum permissible error ratios of 1% and 0.2%, a roughly linear relationship exists between the ratio of hardened layer thickness h_c to electrode distance r_{ele} and the maximum isolation coefficient n_{max}. This relationship can be expressed by the following equations:

$$n_{max,1\%} = 10.30\frac{h_c}{r_{ele}} + 1.04 \quad (11)$$

$$n_{max,0.2\%} = 11.69\frac{h_c}{r_{ele}} + 4.09 \quad (12)$$

According to the numerical simulation inversion results obtained with varying permissible errors, the hardened layer has minimal influence when the apparent resistivity error remains below 1%. Consequently, the hardened layer has a negligible impact on the identification of abnormal bodies. The most optimal scenario occurs when the error approximates 0.2%. Hence, during the selection of the maximum isolation coefficient n_{max}, it is recommended to ensure that the permissible error remains within 1%. This strategy guarantees the accuracy and reliability of the inversion process, facilitating a more precise identification of abnormal bodies.

3.2 Numerical simulations

Fig. 4 illustrates the inversion results of both low- and high-resistivity models, optimized using the ratio method, with h_c set at 1.0 m and h_{top} varying between 1.0, 4.0, and 7.0 m. According to Eq. (11), the correction horizon is established at 11. In the low-resistivity model, the horizontal position and burial depth of the anomaly closely align with the actual target location. The relative resistivity extreme value shows significant improvement, thereby enhancing the identification of the target location, as depicted in Figs. 4(a) and (c). Even when h_{top} reaches 7.0 m (see Fig. 4(e)), despite the inherent limitations of the ERT method in terms of resolution in deeper regions, the optimized inversion results still demonstrate a superior recognition effect compared with the results depicted in Fig. 2(l).

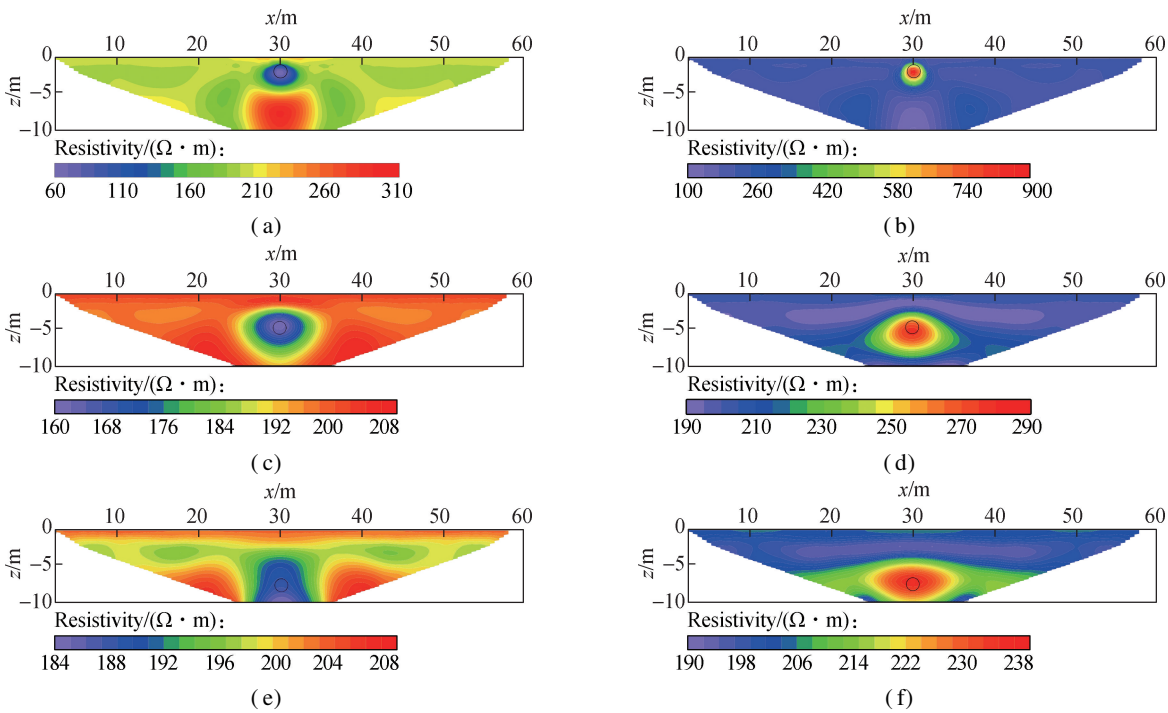

Fig. 4 Inversion results of optimized models of low-resistivity and high-resistivity bodies with varying buried depths. (a) Low-resistivity model for h_{top} = 1.0 m; (b) High-resistivity model for h_{top} = 1.0 m; (c) Low-resistivity model for h_{top} = 4.0 m; (d) High-resistivity model for h_{top} = 4.0 m; (e) Low-resistivity model for h_{top} = 7.0 m; (f) High-resistivity model for h_{top} = 7.0 m

In the case of the high-resistivity model, after compensating for the influence of the hardened layer, the optimized inversion results provide a more precise representation of the actual position, size, and shape of the high-resistivity body, in contrast to Figs. 3(d), (h), (l). This improved depiction is particularly noticeable in Figs. 4(b), (d), (f).

3.3 Laboratory tank modeling

Tank modeling can generate a high density of observations (which is often impractical in field investigations) when coupled with a known geological model with significant a priori information on size, positioning, orientation, and electrical properties; consequently, when a satisfactory experimental technique has been established and any boundary effects compensated, the effectiveness of the ratio method in eliminating the influence of hardened layers can be more effectively evaluated.

The tank model utilized in this study was equipped with the DUK-2A resistivity measurement system manufactured by the Chongqing Geological Instrument Factory. Operat-

ing on a 48 V DC power supply, the system featured a coupling grounding device consisting of a PVC board measuring 2 m × 0.05 m × 0.03 m. Each hole had a diameter of 6 mm, with a center-to-center distance of 0.01 m. To replicate hardened site conditions, C50 strength concrete slabs were employed. These slabs measured 1 m in length, 0.4 m in width, and 0.03-0.06 m in thickness.

The water tank used in this experiment measured 4 m × 1.2 m × 1 m. Data acquisition involved the use of 60 electrodes spaced approximately 0.03 m apart, each with a diameter of 1 mm. To simulate the low resistivity anomaly body, a copper rod was chosen for its superior conductivity. Conversely, a rubber rod of the same diameter was employed to simulate high resistivity owing to its insulating properties.

Using the abovementioned instruments and materials, we established a controlled environment closely resembling field geological conditions. This setup allowed us to accurately evaluate the performance of the ratio method in mitigating the effects of hardened layers.

Fig. 5 illustrates the ERT inversion diagram, contrasting the outcomes of electrodes inserted directly into the water with those employing the coupling device. When electrodes are inserted directly into the water, the water resistivity remains relatively stable, ranging from 12 to 29 Ω · m. However, when the coupling device is used, the inversion results reveal a distinctive two-layer structure, with a layer of high resistivity above and a layer of low resistivity below.

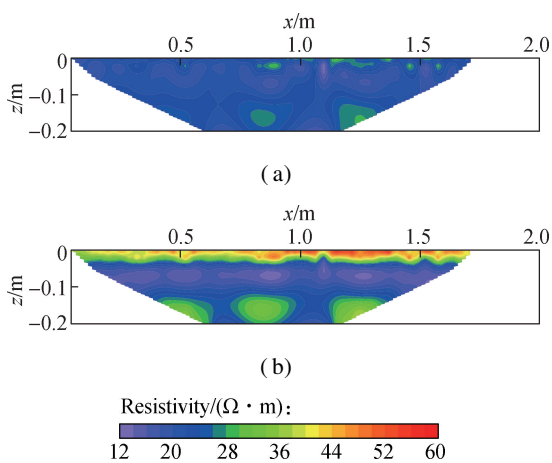

Fig. 5 Inversion results without an abnormal body. (a) Electrode directly inserted into the water; (b) Electrode connected to the concrete

The resistivity of the surface high-resistivity layer ranges from 32 to 57 Ω · m, reflecting the presence of the concrete slab. In contrast, the resistivity range in the lower layer, corresponding to the range observed when the electrode entered the water directly, is 12 to 32 Ω · m. This suggests that the coupling device has minimal impact on the detection results.

The resistivity of the lower layer displays an uneven distribution, which can be attributed to two primary factors. First, the water body may not be entirely uniform. Second, experimental conditions such as temperature, humidity, and water surface fluctuations can introduce instability, thereby contributing to the observed variations in resistivity.

A smaller electrode diameter can significantly increase the variance in grounding resistivity. To address the impact of uneven ground conditions, a maximum permissible error of 0.2% is adopted in determining the n_{max} value in the subsequent discussion. This approach ensures that our analysis remains robust and accurate, even in the presence of potential variations in ground resistivity.

3.3.1 Low-resistivity body model

Figs. 6 and 7 illustrate the ERT inversion results for low- and high-resistivity body models, respectively, following optimization through the ratio method. The results are displayed for various combinations of h_c (0 and 0.03 m) and h_{top} (0.03, 0.12, and 0.21 m).

As depicted in Fig. 6, with h_{top} set at 0.03 m and h_c at 0 m, low-resistivity anomaly appears between 0.82 and 0.9 m, with a burial depth of 0.03 to 0.06 m and resistivity values ranging from 12 to 16 Ω · m. The anomaly presents a nearly circular shape, closely resembling the actual location, shape, and size of the low-resistivity body (see Fig. 6(a)). Conversely, when h_c is set to 0.03 m, the resistivity inversion map depicts a three-layer structure: a high-resistivity surface layer, an intermediate low-resistivity layer, and a deep high-resistivity layer. The surface layer exhibits resistivity values exceeding 500 Ω · m, while the intermediate layer exhibits values ranging from 10 to 300 Ω · m. Closed low-resistivity anomalies are observed at depths of 0.28 to 0.54 m, 0.68 to 1.08 m, and 1.22 to 1.48 m. The deep layer displays resistivity values between 600 and 700 Ω · m. However, the location, size, or shape of the low-resistivity body cannot be determined from the inversion map (see Fig. 6(b)). After the application of the ratio method correction (see Fig. 6(c)), the low-resistivity anomaly appears between 0.78 and 0.96 m, with a burial depth ranging from 0.01 to 0.15 m and resistivity values of 20 to 25 Ω · m. The anomaly maintains a nearly circular shape, aligning well with the occurrence of the low-resistivity body. Notably, the horizontal extent of the low-resistivity anomaly is slightly larger than that observed in the absence of hardening.

When h_{top} is set to 0.12 m, a low-resistivity anomaly is observed between 0.8 and 1.0 m in the absence of a hardened layer. The anomaly's burial depth ranges from 0.08 to 0.21 m, with resistivity values between 17 and 25 Ω · m. Although the anomaly's shape is irregular, it aligns well with the actual position of the low-resistivity body. However, owing to the volume effect, the

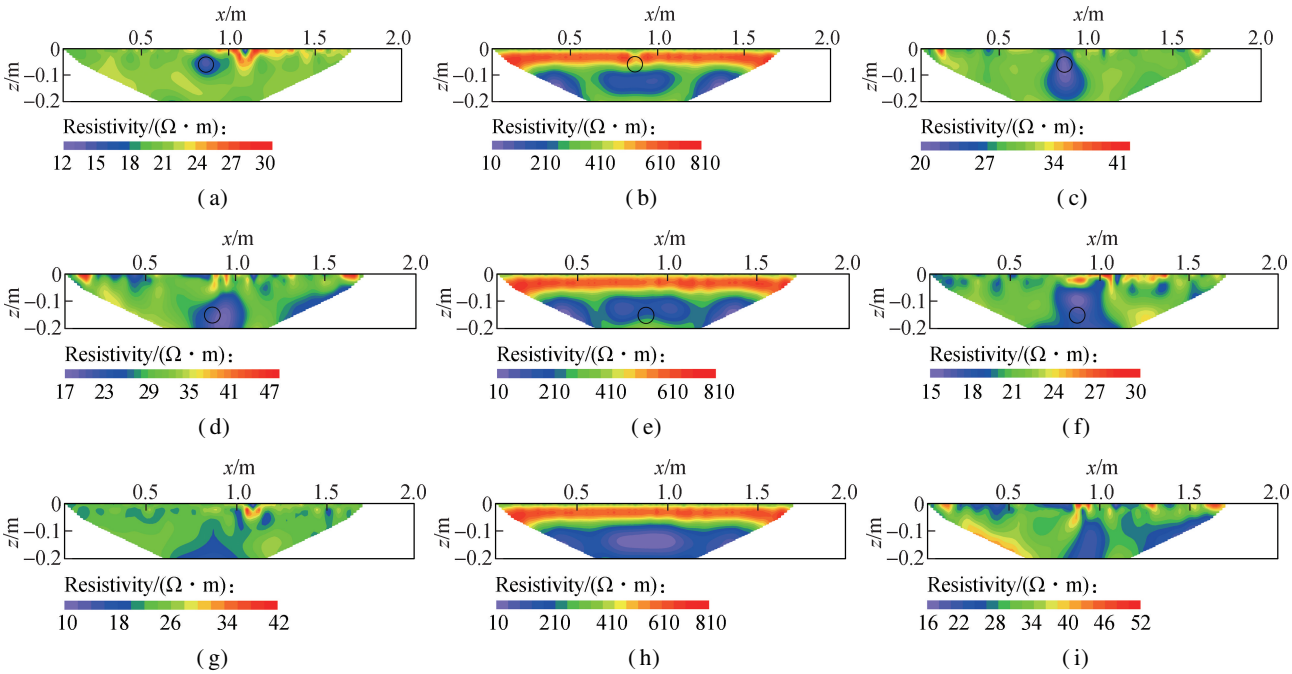

Fig. 6 Tank test results for the low-resistivity body model with varying buried depths. (a) Inversion results for $h_{top}=0.03$ m, $h_c=0$ m; (b) Uncorrected inversion results for $h_{top}=0.03$ m, $h_c=0.03$ m; (c) Corrected inversion results for $h_{top}=0.03$ m, $h_c=0.03$ m; (d) Inversion results for $h_{top}=0.12$ m, $h_c=0$ m; (e) Uncorrected inversion results for $h_{top}=0.12$ m, $h_c=0.03$ m; (f) Corrected inversion results for $h_{top}=0.12$ m, $h_c=0.03$ m; (g) Inversion results for $h_{top}=0.21$ m, $h_c=0$ m; (h) Uncorrected inversion results for $h_{top}=0.21$ m, $h_c=0.03$ m; (i) Corrected inversion results for $h_{top}=0.21$ m, $h_c=0.03$ m

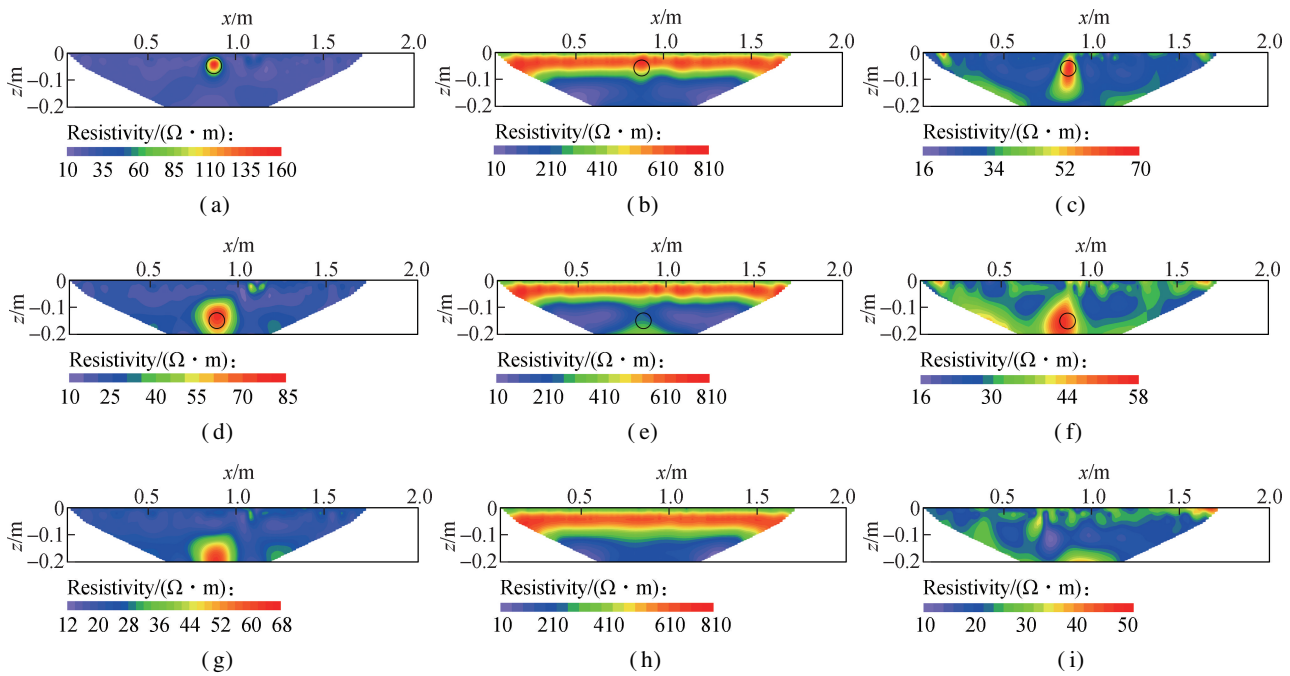

Fig. 7 Tank test results for the high-resistivity body model with varying buried depths. (a) Inversion results for $h_{top}=0.03$ m, $h_c=0$ m; (b) Uncorrected inversion results for $h_{top}=0.03$ m, $h_c=0.03$ m; (c) Corrected inversion results for $h_{top}=0.03$ m, $h_c=0.03$ m; (d) Inversion results for $h_{top}=0.12$ m, $h_c=0$ m; (e) Uncorrected inversion results for $h_{top}=0.12$ m, $h_c=0.03$ m; (f) Corrected inversion results for $h_{top}=0.12$ m, $h_c=0.03$ m; (g) Inversion results for $h_{top}=0.21$ m, $h_c=0$ m; (h) Uncorrected inversion results for $h_{top}=0.21$ m, $h_c=0.03$ m; (i) Corrected inversion results for $h_{top}=0.21$ m, $h_c=0.03$ m

anomaly's extent is larger than the actual size of the low-resistivity body, as shown in Fig. 6(d). At $h_c=0.03$ m (see Fig. 6(e)), the anomaly's basic characteristics are similar to those observed in Fig. 6(b); therefore, further elaboration is omitted. After the application of correction techniques, the low-resistivity anomaly narrows to a

range of 0.76-1.00 m, with a burial depth of 0.05-0.20 m and resistivity values of 15.5-18.5 Ω · m. The shape remains irregular but corresponds to some degree with the actual position of the low-resistivity body. Notably, the extent of the low-resistivity anomaly is larger than that at $h_c = 0$ m (see Fig. 6(f)).

At $h_{top} = 0.21$ m, in the absence of a hardened layer, the low-resistivity anomaly appears between 0.66 and 1.06 m. The burial depth of the anomaly exceeds 0.18 m, with resistivity values ranging from 10 to 16 Ω · m, aligning well with the actual position. However, owing to the volume effect, the extent of the anomaly is significantly larger than the actual body, as seen in Fig. 6(g). With a 0.03 m-thick hardened layer, the inversion map exhibits a three-layer structure: a high-resistivity surface layer (750 Ω · m), an intermediate low-resistivity layer (10-100 Ω · m), and a deep high-resistivity layer (250-400 Ω · m). The low-resistivity anomaly occurs between 0.64 and 1.10 m. However, accurately correlating the position, size, and shape of the low-resistivity anomaly with the actual body is not feasible, as shown in Fig. 6(h). Upon the application of correction techniques, a relatively low-resistivity region emerges between 0.82 and 1.20 m, with a burial depth of 0.10-0.23 m. The resistivity values within this region range from 16 to 24 Ω · m, forming an olive-shaped pattern. Notably, the central position of the anomaly is shallower than the actual position of the low-resistivity body, and the extent of the low-resistivity anomaly is larger than the actual size of the low-resistivity body, as illustrated in Fig. 6(i).

3.3.2 High-resistivity body model

For high-resistivity bodies, when h_{top} is set to 0.03 m, the position, size, and shape of the high-resistivity body cannot be determined from the uncorrected direct inversion results (see Fig. 7(b)). However, after the application of the correction techniques, the high-resistivity anomaly is observed between 0.82 and 0.92 m. The anomaly has a burial depth ranging from 0.02 to 0.15 m and exhibits resistivity values between 46 and 70 Ω · m. The anomaly exhibits a teardrop shape closely corresponding to the actual position, shape, and size of the high-resistivity body (see Fig. 7(c)).

At $h_{top} = 0.12$ m, the uncorrected resistivity inversion map reveals a three-layer structure: a high-resistivity layer at the surface with resistivity values exceeding 250 Ω · m, an intermediate layer with resistivity values of 220-420 Ω · m, and a relatively high-resistivity layer at the bottom with resistivity values of ~600 Ω · m. The actual position of the high-resistivity body aligns with the region of relatively high resistivity within the intermediate layer. However, the size and shape of the high-resistivity body cannot be accurately determined, and its existence cannot be discerned from the inversion map (see Fig. 7(e)). After correction, the high-resistivity anomaly is observed to extend horizontally between 0.74 and 0.90 m, with a burial depth ranging from 0.09 to 0.21 m. The resistivity values fall between 40 and 50 Ω · m, and the anomaly exhibits a teardrop shape. The shape corresponds well with the actual position and shape of the high-resistivity body, although the extent of the high-resistivity anomaly is larger than the actual size of the high-resistivity body (see Fig. 7(f)).

At $h_{top} = 0.21$ m, the corrected inversion results also effectively pinpoint the location of the high-resistivity body. However, when h_c reaches 0.06 m, even after correction, a low-resistivity cylinder with a diameter of 0.06 m becomes completely undetectable. Similarly, the anomaly caused by a high-resistivity cylinder of the same size is relatively weak, making it challenging to determine the existence of the high-resistivity anomaly.

In the inversion results of high-resistivity models, when h_{top} exceeds 0.12 m (corresponding to Figs. 7(f) and (i)), the corrected inversion outcomes show uneven resistivity distribution around the high-resistivity anomaly. This unevenness is attributed to a decline in the signal-to-noise ratio due to an increase in burial depth.

According to the abovementioned experimental results, the exploration effectiveness of the ERT method under hardened ground conditions correlates with the ratio of electrode spacing to hardened layer thickness or the ratio of detection depth to hardened layer thickness. When the ratio of hardened layer thickness to electrode spacing is not greater than 1, different buried anomalies are reflected to varying degrees in the results obtained from the direct inversion of ERT data. After the application of correction using the ratio method, anomalies at different burial depths become identifiable, although with a somewhat expanded anomaly range compared with conditions without a hardened layer. However, when the ratio of hardened layer thickness to electrode spacing reaches 2 or higher, discerning anomalies becomes challenging, regardless of the application of correction or not.

4 Field Survey Example

4.1 Location and geological conditions of the study area

The study area is located at the convergence of the hilly terrain in southern Anhui and the flat marshland plains in the middle and lower reaches of the Yangtze River. Bordered by hills on three sides, the area features rivers meandering through the marshland, creating a relatively level landscape. Typically, the ground elevation in the marshland varies from 12.0 to 16.0 m, with dike crests ranging from 17.0 to 20.7 m and dike heights between 3 and 6 m. A network of channels and ditches intersects the marshland.

The study area's stratigraphy falls within the Guichi

stratigraphic subarea of the Yangtze River coastal zone. The overlying strata comprise loose alluvial and diluvial deposits. Toward the surface, there is a prevalence of recently deposited clayey soil, silty soil, and occasionally silty-sandy soil. In the middle, there are layers of alluvial and diluvial sand and gravel, while the lower portion consists of residual deposits. The underlying bedrock is cretaceous siltstone and other bedrock formations. The intricate network of canals and ditches often leads to localized thinning or absence of the upper strata, exposing the sand and gravel layers directly in ponds. The soil composition within the study area predominantly comprises medium-to heavy-silty loam, heavy-silty loam, clay with gravel, sand and gravel with clay, and distinct layers of sand and gravel, with residual deposits underlying them. Siltstone forms the bedrock at the bottom. According to engineering geological characteristics, especially soil permeability, the soil layers can be divided into two major categories: sandy soils, encompassing sandy loam, sand and gravel with clay, and pure sand and gravel layers, characterized by moderate to strong permeability; and clayey soils, including silty loam and silty soils, which exhibit weak to slightly permeable characteristics.

The predominant groundwater type in the site is pore-confined water. The primary aquifer comprises sand and gravel interspersed with clay, lying beneath a layer of clayey soil(acting as a relative aquitard). Typically, the aquifer thickness ranges from 5.0 to 8.0 m, characterized by abundant water content. Portions of this sand and gravel layer are exposed within the river channel owing to deep riverbed incision. The groundwater level fluctuates in tandem with variations in river water level. During the dry season, groundwater levels slightly surpass those of the river, leading to discharge into the river. During the flood season, the river water level exceeds that of the groundwater, replenishing it from the river. Throughout the study period, the stable groundwater level in the exploration holes ranged from approximately 13.06 to 12.46 m, while the Huangpen River's water level averaged 12.74 m. This indicates a minor disparity between the river and groundwater levels.

4.2 Data acquisition

During on-site data collection, if the grounding resistance exceeds 2 000 Ω, salt water is applied to the electrodes to enhance grounding conditions. In areas featuring cement pavement or exposed bedrock, electrodes are inserted into the RH-1 electrode coupling device[33], which is then filled with concentrated salt water. The measurement point is subsequently covered with a mixture of concentrated salt water and mud, ensuring thorough contact with the pavement. The coupling device is placed atop the measurement point and moistened with salt water again. Measurements are conducted at least twice, with a maximum repeat error of 2% controlled. Throughout the detection process, grounding resistance typically ranges from 200 to 800 Ω when electrodes are embedded into the soil. When a grounding can is applied to the soil, the grounding resistance typically falls between 200 and 1 000 Ω. Conversely, when a grounding can is placed on the hardened pavement, the grounding resistance usually ranges from 1 000 to 2 500 Ω. Lines 1 and 2 run parallel to each other and are spaced approximately 0.3 m apart.

4.3 Data interpretation and result analysis

Fig. 8(a) presents the inversion results of survey line 2, while Figs. 8(b) and (c) show the direct and post-correction outcomes of survey line 1 on the hardened pavement, respectively. The uncorrected inversion results for survey line 1 (see Fig. 8(b)) demonstrate a three-layer structure of high-low-high, similar to the adjacent survey line 2. However, there are discrepancies in layer delineation, with local stratigraphic variations of 3-5 m (see Fig. 9). Conversely, the corrected inversion results (see Fig. 8(c)) exhibit a substantial alignment with survey line 2 (see Fig. 9). This alignment underscores the accuracy and reliability of the corrected inversion outcomes.

According to the provided data, the following interpretations can be made:

Layer ① is characterized by relatively high resistivity, ranging from 80 to 250 Ω · m, with a thickness of 2 to 3 m.

Layer ②, situated at depths of 3 to 10 m, exhibits resistivity values of 28-80 Ω · m, indicating a low-resistivity layer.

Layers ③ and ④ demonstrate relatively high resistivity, with values of 80-520 Ω · m and extending beyond 10 m in depth. When the depth exceeds 12 m, resistivity values exceed 500 Ω · m.

In alignment with geological observations, throughout the exploration phase, the consistent depth of the groundwater level in the exploration boreholes ranges from approximately 2.94 to 3.54 m. The water level depth of the Huangpen River during the same period measures 3.26 m. According to these findings, it is assumed that the boundary between Layers ① and ② represents the groundwater level, situated at depths of 2-4 m. Similarly, the demarcation between Layers ③ and ④ aligns with the bedrock surface found at depths exceeding 10 m.

Layer ①, situated above the groundwater level, is less susceptible to leakage or other hazards. Layer ②, mainly consisting of silty loam mixed with sandy soil, displays weak permeability and low resistivity in the inversion map. This layer is most susceptible to leakage hazards within the dike. Layers ③ and ④, characterized by high resistivity and primarily composed of sandstone, exhibit continuous layering without significant anomalies.

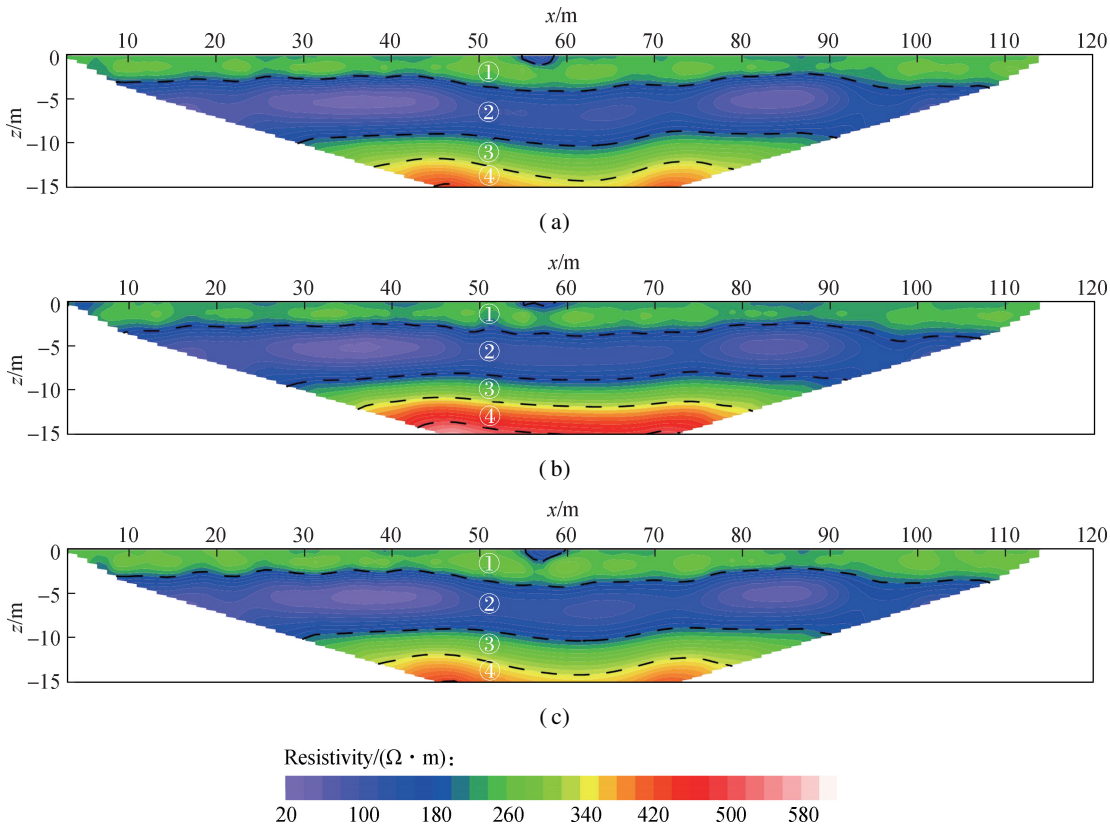

Fig. 8 Field results of the study area. (a) Inversion result map of survey line 2; (b) Direct inversion result map of survey line 1 without correction; (c) Inversion result map of survey line 1 after correction through the ratio method

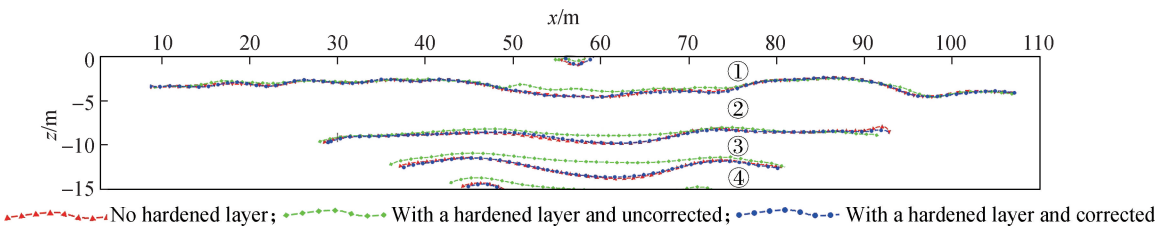

Fig. 9 Diagram of stratigraphic division and comparison

5 Conclusions

1) The hardened layer does not notably affect the identification of shallow anomalies of a certain size. However, as the burial depth of the anomaly increases, the shielding effect of the hardened layer increases the volume effect of the ERT method, causing a rapid decline in anomaly detection capability with increasing burial depth.

2) The findings from numerical simulations and tank experiments using both low- and high-resistivity models demonstrate the effectiveness of the ratio method based on distortion principles for mitigating the impact of hardened layers. During the determination of the maximum isolation coefficient n_{max}, maintaining an allowable error below 1% is necessary. In ERT exploration conducted under hardened site conditions, the capability to detect abnormal bodies is notably enhanced at a hardened layer thickness to electrode spacing ratio of $\leqslant 1$. Correction and optimization through the ratio method yield reliable results. However, when the hardened layer thickness exceeds twice or more the electrode spacing, accurately identifying target abnormal bodies through corrected inversion results becomes challenging.

3) The case study of flood control engineering exploration in the Zhangxi section of the Huangpen River in Dongzhi County demonstrates that the detection effect after correction with the ratio method is comparable to that for adjacent unhardened road surfaces.

References

[1] Dahlin T. The development of DC resistivity imaging techniques[J]. *Computers & Geosciences*, 2001, **27**(9): 1019 − 1029. DOI: 10.1016/S0098-3004(00)00160-6.

[2] Shima H, Sakayama T. Resistivity tomography: An approach to 2-D resistivity inverse problems [C]//*SEG Technical Program Expanded Abstracts* 1987. New Orleans, American, 1987: 59 − 61. DOI: 10.1190/1.

1892038.

[3] Li Z W, Zhou Y Y, Feng R. Data-collecting system for resistivity tomography [J]. *Progress in Geophysics*, 2004, **19**(4): 812 − 818. DOI: 10.3969/j. issn. 1004-2903. 2004. 04. 019. (in Chinese)

[4] Zhe J P, Greenhalgh S, Marescot L. Multichannel, full waveform and flexible electrode combination resistivity-imaging system[J]. *Geophysics*, 2007, **72**(2): F57 − F64. DOI: 10.1190/1.2435081.

[5] Jiang L C. *Optimization and preliminary application of electrode random distributed high-density electrical exploration design*[D]. Hangzhou: Zhejiang University, 2021. (in Chinese)

[6] Pan H X, Lü X Y, Wang Z G, et al. Microelectrode array for bioelectrical signal stimulation and recording[J]. *Journal of Southeast University* (*English edition*), 2011, **27**(4): 361 − 366. DOI: 10. 3969/ j. issn. 1003-7985. 2011. 04. 003.

[7] Wu J F, Yu Z Z, Li J Q, et al. Transmission cable fault detector based on waveform reconstruction[J]. *Journal of Southeast University*(*English edition*), 2013, **29**(1): 48 − 51. DOI: 10. 3969/ j. issn. 1003-7985. 2013. 01. 010.

[8] Huang J G, Ruan B Y, Wang J L, et al. Study on the anomalous characteristics of the drilling surface electrode combined resistivity observation device[J]. *Journal of Geophysics*, 2009, **52**(5): 1348 − 1362. DOI: 10.3969/ j. issn. 0001-5733. 2009. 05. 025. (in Chinese)

[9] Zhao G M, Li T L, Xu K J, et al. The study and application of well-surface resistivity method in the safety at coal field[J]. *Progress in Geophysics*, 2007, **22**(6): 1895 − 1899. DOI: 10. 3969/j. issn. 1004-2903. 2007. 06. 034. (in Chinese)

[10] Slater L, Binley A M, Daily W, et al. Cross-hole electrical imaging of a controlled saline tracer injection[J]. *Journal of Applied Geophysics*, 2000, **44**(2/3): 85 − 102. DOI: 10.1016/S0926-9851(00)00002-1.

[11] Coscia I, Greenhalgh S A, Linde N, et al. 3D crosshole ERT for aquifer characterization and monitoring of infiltrating river water[J]. *Geophysics*, 2011, **76**(2): G49-G59. DOI: 10.1190/1.3553003.

[12] Hafiz M, Hakhoo N, Bhat G, et al. An assessment of the source potential and reservoir characterization for tight gas exploration in the Subathu Formation shale, Himalayan Foreland Basin, Northwestern India[J]. *Journal of Asian Earth Sciences*, 2022, **230**: 105205. DOI: 10.1016/j. jseaes. 2022. 105205.

[13] Legault J M, Carriere D, Petrie L. Synthetic model testing and distributed acquisition dc resistivity results over an unconformity uranium target from the Athabasca Basin, northern Saskatchewan[J]. *The Leading Edge*, 2008, **27**(1): 46 − 51. DOI: 10.1190/1.2831679.

[14] Ma F S, Di Q Y, Li K P, et al. Application of high-density resistivity method in detecting water-bearing structures at a seabed gold mine[J]. *Chinese Journal of Geophysics*, 2016, **59**(12): 4432 − 4438. (in Chinese)

[15] Şener A, Pekşen E, Yolcubal İ. Application of square array configuration and electrical resistivity tomography for characterization of the recharge area of a Karst aquifer: A case study from Menekşe Karst Plateau (Kocaeli, Turkey)[J]. *Journal of Applied Geophysics*, 2021, **195**: 104474. DOI: 10.1016/j. jappgeo. 2021. 104474.

[16] Rucker D F. Enhanced resolution for long electrode ERT[J]. *Geophysical Journal International*, 2012, **191**(1): 101 − 111. DOI: 10.1111/j. 1365-246x. 2012. 05643. x.

[17] Shang T X, Xu Z W, Gong X L, et al. Application of electrical sounding to determine the spatial distribution of groundwater quality in the coastal area of Jiangsu Province, China[J]. *Journal of Hydrology*, 2021, **599**: 126348. DOI: 10.1016/j. jhydrol. 2021. 126348.

[18] Zhang H F, Ma S Q, Liang Y, et al. Detection of internal voids in underwater riprap based on resistivity tomography scanning[J]. *Journal of Hohai University* (*Natural Sciences*), 2023, **51**(4): 123 − 128. DOI: 10. 3876/j. issn. 10001980. 2023. 04. 016. (in Chinese)

[19] Kong F L, Xu C, Li J. The application of high-density electrical method in the detection of hidden dangers in a dam of a reservoir in Xinjiang[J]. *Chinese Journal of Engineering Geophysics*, 2022, **19**(1): 16 − 20. DOI: 10. 3969/j. issn. 1672-7940. 2022. 01. 003. (in Chinese)

[20] Fan B S, Guo C C. The application of high-density electrical method in reservoir leakage detection[J]. *Journal of the Yangtze River Academy of Sciences*, 2019, **36**(10): 165 − 168. DOI: 10. 11988/ckyyb. 20190940. (in Chinese)

[21] Xu Z, Yang J J, Liu R B, et al. Identification of underground freshwater bodies in coastal areas based on high-density electrical method[J]. *Frontiers of Marine Geology*, 2022, **38**(6): 47 − 53. DOI: 10. 16028/j. 1009-2722. 2021. 205. (in Chinese)

[22] Chu Y, Cai G J, Liu S Y, et al. Review of the electrical conduction model of rock and soil medium[J]. *Journal of Southeast University* (*Natural Science Edition*), 2023, **53**(5): 926 − 938. DOI: 10.3969/j. issn. 1001-0505. 2023. 05. 020.

[23] Zhang Y M, Bao F, Tong Z, et al. Radar wave response of slab bottom voids in heterogeneous airport concrete pavement[J]. *Journal of Southeast University* (*Natural Science Edition*), 2023, **53**(1): 137 − 148. DOI: 10. 3969/j. issn. 1001-0505. 2023. 01. 017.

[24] Chen S, Li Y Q, Li T H, et al. Application of high density resistivity method to urban geological survey in Urumqi[J]. *Xinjiang Geology*, 2019, **37**(1): 28 − 33. DOI: 10.3969/j. issn. 1000-8845. 2019. 01. 005. (in Chinese)

[25] Wu H, Yin Y F, Jin W L. Exploration of the application of high-density electrical method in urban subsidence areas of Zhengzhou[J]. *Mineral Exploration*, 2022, **13**(12): 1811 − 1817. DOI: 10. 20008/j. kckc. 202212009. (in Chinese)

[26] Guo C C, Yang J C, Shi M S, et al. Application of high density electrical method in detection of polymer cutoff wall[J]. *Progress in Geophysics*, 2019, **34**(2): 709 − 716. (in Chinese)

[27] Jian X X, Wang X B, Yang L R, et al. Terrain influence correction using high-density resistivity method[J]. *Computing Techniques for Geophysical and Geochemical Exploration*, 2008, **30**(4): 303 − 307. DOI: 10.3969/j. issn. 1001-1749. 2008. 04. 009. (in Chinese)

[28] Li Q C, Guo L. Theory and practice on the apparent resistivity method and the apparent ratio parameter method

[J]. *Progress in Geophysics*, 2019, **34**(1): 326 – 330. DOI: 10.6038/pg2019BB0181. (in Chinese)

[29] Yang T W, Huang J G, Xu R H, et al. Research on improving the resolution of deep anomalies through multi-scale inversion in high-density electrical methods[J]. *Chinese Journal of Engineering Geophysics*, 2013, **10**(3): 369 – 373. DOI: 10.3969/j.issn.1672-7940.2013.03.017. (in Chinese)

[30] Loke M H, Acworth I, Dahlin T. A comparison of smooth and blocky inversion methods in 2D electrical imaging surveys[J]. *Exploration Geophysics*, 2003, **34**(3): 182 – 187. DOI: 10.1071/eg03182.

[31] Yu X J, Miao L C, Liu S Y. The electrical resistivity characteristics of cement-soil and flyash-lime-soil [J]. *Journal of Southeast University* (*English Edition*), 2001, **17**(1): 55 – 58. DOI: 10.3969/j.issn.1003-7985.2001.01.013.

[32] Li M L, Qian J S, Wang L X, et al. Exploration of electrical resistivity evaluation method for concrete curing effect[J] *Journal of Building Materials*, 2011, **14**(4): 473 – 477. DOI: 10.3969/j.issn.1007-9629.2011.04.007. (in Chinese)

[33] Jiang F Y. A grounding device for high-density electrical method: CN213845536U [P]. 2021-07-30. (in Chinese)

基于比值法的硬化场地电阻率层析成像法数据优化

蒋甫玉[1]　高丽坤[2]　陈海军[3]　倪　炯[1]　李富强[4]

([1]河海大学地球科学与工程学院, 南京 211100)

([2]江苏省地质矿产局第一地质大队, 南京 210041)

([3]南京水利科学研究院, 南京 210029)

([4]中国能源建设集团湖南省电力设计院有限公司, 长沙 410007)

摘要:为减弱硬化层的屏蔽效应对电阻率层析成像的影响,在探讨具有不同电阻率大小、不同厚度的混凝土硬化层对目标体探测影响的基础上,提出了一种考虑隔离系数的基于畸变校正原理的比值法.数值模拟试验和室内水槽试验结果表明,利用比值法对原始采集数据进行校正处理时,选择的最大隔离系数允许误差应当不大于1%.硬化层厚度与电极距的比值不大于1时,经比值法校正后,能明显地提升对目标体赋存状态的识别能力;但当硬化层厚度达到2倍电极间距及以上时,比值法亦不能达到较好的效果.东至县张溪河段黄溢河防洪治理工程探测实例表明,经比值法校正后的探测效果与邻近未硬化路面相当,明显削弱了硬化层的影响,得到了更为可靠的成果.

关键词:比值法;电阻率层析成像;硬化场地;畸变原理;数据优化

中图分类号:P631